
Article:
Farias Martins, L., Stone, D. orcid.org/0000-0002-5770-3917 and Foster, M. orcid.org/0000-0002-8565-0541 (2020) Modelling of phase-shift modulated bidirectional CLLC resonant converter. IET Power Electronics, 13 (12). pp. 2628-2637. ISSN 1755-4535

https://doi.org/10.1049/iet-pel.2018.5672

Modelling of Phase-Shift Modulated Bidirectional CLLC Resonant Converter

Lais Farias Martins [1], David Stone [1*], Martin Foster [1]

[1] Department of Electronic and Electrical Engineering, University of Sheffield, Sir Frederick Mappin Building, Mappin Street, Sheffield, United Kingdom, S1 3JD
[*] d.a.stone@sheffield.ac.uk

Abstract: The paper proposes the application of two modelling techniques for analysis of bidirectional CLLC resonant converters. The state-variable and cyclic-averaging techniques are applied for converters operating under two types of phase-shift modulation: single-phase-shift (SPS) and pulse-phase modulation (PPM). The converter is analysed considering forward and reverse power flow directions and a state-variable equation description is obtained for both modes. The models are first validated through simulation, comparing the state-variable and cyclic-averaging results to a Spice-based simulation. Additionally, a low power prototype is built, experimental results are presented and the influence of parasitic elements and system delays is discussed. Simulation and experimental results show the models can accurately represent the behaviour of CLLC converters for both types of phase-shift modulation. In addition, using the cyclic-averaging technique results in a considerably faster execution compared to state-variable and Spice-based models.

1. Introduction

The interest in electric vehicles (EVs) has been increasing especially due to environmental reasons, development of technology and government incentives, resulting in increased affordability. The vehicle-to-grid (V2G) technology was introduced from concerns about possible grid overload and stability problems originating from a large EV population. Most battery chargers for EVs are unidirectional; however, a V2G system enables bidirectional power flow between grid and battery. Consequently, the battery may function as support to the grid at peak times, when the energy demand is high, contributing to grid stability and efficient use of energy. Typical bidirectional chargers for V2G consist of an AC-DC converter for power factor control and a DC-DC converter for output voltage and current regulation [1].

The Dual Active Bridge (DAB) is a widely used topology of bidirectional DC-DC converter for V2G applications [2–4]. Due to the DAB limitations such as large reactive current, limited voltage operating range and reduced efficiency, complex modulation techniques and control strategies [2, 5, 6] have to be adopted resulting in difficult implementation. Resonant variants of the DAB as the series-resonant DAB (SRDAB), LLC and CLLC converters were proposed to obtain improved operation.

The SRDAB and DAB are compared in [7] and although the resonant topology presents better efficiency both topologies have weak performance for wide voltage range operation. The LLC converter is an improved topology for battery chargers with high efficiency, high power density and low electromagnetic interference (EMI) [8–11]. Due to loss of soft switching operation during reverse mode, the LLC topology is more suitable for unidirectional power transfer [12].

The CLLC converter, shown in Fig. 1, is a 4th order resonant topology that provides reduced switching losses, high efficiency and operation under wide voltage range. A considerable advantage of the CLLC converter is the easily achieved soft switching operation for forward and reverse modes under frequency modulation [13, 14].

Two modes of operation are possible for a bidirectional converter: in forward mode the power flows from the DC bus, to the battery, while in reverse mode the battery serves as a supply to the grid and the power flows from the battery to the DC bus.

To date, most literature focuses on frequency modulated CLLC converters [1, 12, 15, 16]. However, for applications requiring fixed-frequency operation phase-shift modulation can be implemented as an alternative [13, 14, 17].

This paper investigates a CLLC bidirectional converter operating under two types of phase-shift modulation: single phase-shift (SPS) and pulse-phase modulation (PPM). In this study two modelling techniques for time-domain analysis of the converter are applied: state-variable and cyclic-averaging. A linear state-variable model using dq transformation for CLLC converters was proposed in [13]. Here, a simpler piecewise linear state-variable model is proposed and will serve as base for the implementation of the cyclic-averaging method.

The cyclic-averaging technique was proposed in [18] as an accurate method of time-domain analysis for periodically switched systems. The steady–state values of the state-variables are obtained from analytical equations without the requirement for integration of the underlying differential equations. Therefore, steady-state prediction is obtained rapidly when compared with integration-based methods. Previously, cyclic-averaging has been used to analyse LLC converters [11] and LCC converters [19]. In [20], a simulation study was performed for CLLC converters operating under SPS modulation, here then, this is extended to apply cyclic-averaging analysis to 4th order CLLC converters operating under both types of phase-shift modulation, SPS and PPM, using experimental and simulation results for validation.

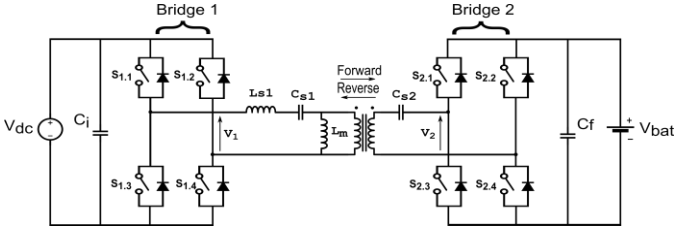

Fig. 1 CLLC bidirectional resonant converter topology

The paper is structured as follows. In Section 2, the modulation techniques analysed in this paper will be explained. The state-variable model is presented in Section 3. The cyclic-averaging model is described in Section 4. Section 5 contains the converter design and analysis of simulation and experimental results.

2. Phase-shift modulation technique

Two cases of phase-shift modulation are considered in this paper for the CLLC converter analysis, the first and simpler method of phase-shift modulation is the Single Phase-Shift (SPS) [21–23]. In this configuration, shown in Fig. 2, the frequency is fixed, duty cycle is kept at 50% and a phase-shift (ϕ) is imposed between the output voltages of the two H-bridges v_1 and v_2, shown in Fig. 1. The phase-shift angle ($-90° \leq \phi \leq 90°$) is used to control the output power and the power flow direction is determined by the sign of the angle between v_1 and v_2, where positive values result in forward mode operation and negative values are used when operating in reverse mode. The maximum power transfer is reached at 90° for forward mode or -90° for reverse mode.

One drawback of SPS modulation is the large reactive currents and conduction losses that occur under partial loading [14, 17], therefore, we also analyse CLLC converters behaviour when operating under Pulse-Phase modulation (PPM) [24, 25]. Note that PPM is also known as Triple Phase-Shift (TPS) modulation as in [13, 17].

The typical waveforms for operation under PPM modulation are represented in Fig. 3, where $v_{s1.3}$ and $v_{s1.4}$ are the drain-source voltages of MOSFET switches S1.3 and S1.4 from Fig. 1. The frequency is still fixed and the output power can still be controlled by the angle between the two bridge voltages (ϕ). In addition, the duty cycles of bridge 1 (α_1) and bridge 2 (α_2) are also control variables thus providing a greater fidelity of control and the ability to reduce reactive currents. The additional control angles α_1 and α_2 have a range from 0 to 180°.

In most applications the angle ϕ is fixed at ±90°, depending on the desired power flow direction, thereby maintaining unity power factor, and α_1 is kept equal to α_2 for a simpler control and higher efficiency.

3. State-variable analysis

To obtain the state-variable description the equivalent circuits obtained from the converter presented in Fig. 1 will be analysed for operation in forward and reverse modes. For this analysis, the circuit from Fig. 1 is divided into two sub-systems. The resonant network is considered the fast subsystem and the output filter, due to its slow response constitutes the slow sub-system, with these two sets of state-variable equations being connected by a coupling equation that represents the non-linear behaviour of the output bridge.

The equivalent circuits for state-variable analysis in forward and reverse mode are presented in Fig. 4.

For operation under SPS modulation the voltages generated by the two full-bridges are square waves represented as v_1 and nv_2, where n= N_1/N_2 is the transformer's turns ratio with N_1 and N_2 being the number of turns on primary and secondary windings respectively.

The bridge voltages considering SPS modulation are given based on battery and DC link voltage as in (1) and (2).

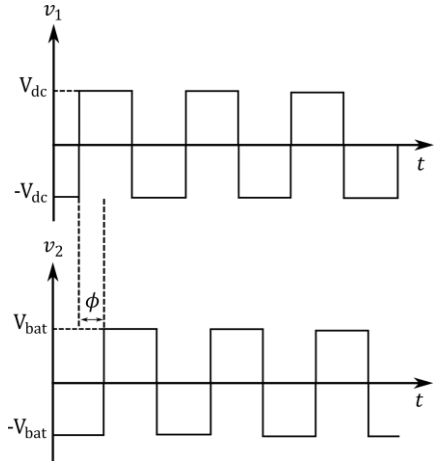

Fig. 2 Bridge output voltages for SPS modulation, operating in reverse mode

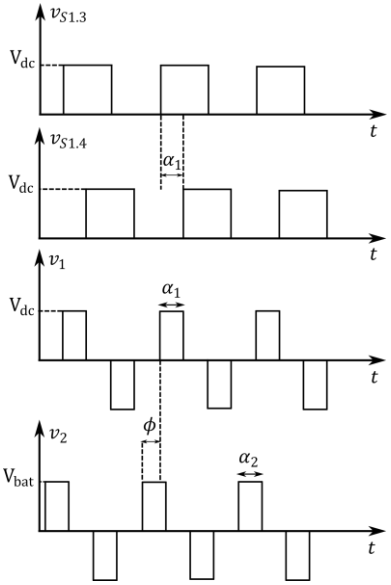

Fig. 3 Bridge output voltages for PPM modulation, operating in forward mode

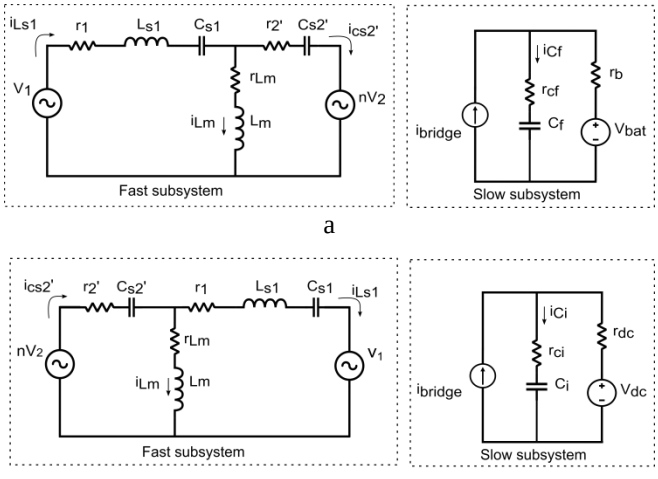

Fig. 4 Equivalent circuit for state-variable analysis
(a) Forward mode, **(b)** Reverse mode

$$v_1(t) = \pm V_{dc} \tag{1}$$

$$v_2(t) = \pm V_{bat} \tag{2}$$

As seen in Fig. 3, for PPM modulated converters a zero voltage level is added to v_1 and v_2.

For forward operation, the fast subsystem is referred to the primary while the slow is referred to the secondary. Using basic circuit analysis, the state-variable description for the fast subsystem in forward mode can be obtained:

$$\frac{di_{Ls1}}{dt} = \frac{v_1 - (r_1 + r_2')i_{Ls1} - v_{Cs1} + r_2' i_{Lm} - v_{Cs2'} - nv_2}{L_{s1}} \tag{3}$$

$$\frac{dv_{Cs1}}{dt} = \frac{i_{Ls1}}{C_{s1}} \tag{4}$$

$$\frac{di_{Lm}}{dt} = \frac{r_2' i_{Ls1} - (r_{Lm} + r_2')i_{Lm} + v_{Cs2'} + nv_2}{L_m} \tag{5}$$

$$\frac{dv_{Cs2'}}{dt} = \frac{i_{Ls1} - i_{Lm}}{C_{s2'}} \tag{6}$$

The slow subsystem is described as:

$$\frac{dv_{Cf}}{dt} = \frac{V_{bat} + r_b i_{bridge} - v_{Cf}}{C_f(r_b + r_{Cf})} \tag{7}$$

The coupling equation is obtained considering the operation of the active bridge on the output side:

$$i_{bridge} = \begin{cases} n(i_{Ls1} - i_{Lm}) \; when \; v_2(t) > 0 \\ -n(i_{Ls1} - i_{Lm}) \; when \; v_2(t) < 0 \\ 0 \; when \; v_2(t) = 0 \end{cases} \tag{8}$$

The case of $v_2(t)$ equal to zero only occurs for PPM modulation.

Considering the opposite power flow direction, the state-variable description is obtained based on the equivalent circuit of Fig. 4b. Since the output is now on the primary side both fast and slow subsystems are referred to the primary.

$$\frac{di_{Ls1}}{dt} = \frac{nv_2 - (r_1 + r_2')i_{Ls1} - v_{Cs1} - r_2' i_{Lm} - v_{Cs2'} - v_1}{L_{s1}} \tag{9}$$

$$\frac{dv_{Cs1}}{dt} = \frac{i_{Ls1}}{C_{s1}} \tag{10}$$

$$\frac{di_{Lm}}{dt} = \frac{nv_2 - r_2' i_{Ls1} - (r_{Lm} + r_2')i_{Lm} - v_{Cs2'}}{L_m} \tag{11}$$

$$\frac{dv_{Cs2'}}{dt} = \frac{i_{Ls1} + i_{Lm}}{C_{s2'}} \tag{12}$$

The slow subsystem is described as:

$$\frac{dv_{Ci}}{dt} = \frac{V_{dc} + r_{dc} i_{bridge} - v_{Ci}}{C_i(r_{dc} + r_{Ci})} \tag{13}$$

The coupling equation is given by:

$$i_{bridge} = \begin{cases} i_{Ls1} \; when \; v_1(t) > 0 \\ -i_{Ls1} \; when \; v_1(t) < 0 \\ 0 \; when \; v_1(t) = 0 \end{cases} \tag{14}$$

The case of $v_1(t)$ equal to zero only occurs for PPM modulation.

4. Cyclic-averaging analysis

Cyclic-averaging is a technique used to model periodically switching systems, as an alternative to state-space averaging and traditional methods based on integration techniques. For switching power converters, the traditional steady-state condition does not exit owing to the constant switching nature of the system. Therefore, the notion of a cyclic-mode is used to represent the steady-state condition. A system is said to be operating in a cyclic-mode when the final condition of a cycle is equal to the initial condition for that cycle. Thus, cyclic-averaging is the average of state-variables over a cyclic-mode using the method proposed in [18].

The CLLC system presented in this paper is considered cyclic because the state-vector at the beginning and at the end of the switching period is equal, therefore:

$$x(t) = x(t + mT) \tag{15}$$

where T is the period of the input voltage and m is an integer representing the number of cycles.

Based on the switches states, a single cycle of operation can be divided into operation modes resulting in a set of piecewise linear equations. Each mode i has the following state-variable representation:

$$\dot{x}(t) = A_i x(t) + B_i \tag{16}$$

where $x(t)$ is the state vector, A_i is the dynamic matrix and B_i is the excitation term.

Equation (16) can be solved analytically for each operation mode using the following equation:

$$x(t) = e^{A_i(t - t_{i-1})} x(t_{i-1}) + \int_{t_{i-1}}^{t} e^{A_i(t-\tau)} B_i d\tau \tag{17}$$

Here, the circuit operates in each mode for a fixed period. The normalised time interval for each mode is given by a duty cycle d_i. If T is the period of a cycle, the circuit operates in mode i for $d_i T$ seconds. The following notation is used for every mode:

$$\phi_i = \phi(t_i, t_{i-1}) = e^{A_i(t_i - t_{i-1})} = e^{A_i d_i T} \tag{18}$$

$$\begin{aligned} \Gamma_i &= \int_{t_{i-1}}^{t_i} e^{A_i(t_i - \tau)} B_i d\tau \\ &= (e^{A_i d_i T} - I) A_i^{-1} B_i, \; A_i \text{ is invertible} \end{aligned} \tag{19}$$

Analytical solution of the system is possible but complex, especially for cases where A_i is singular.

Here, the augmented state vector technique is used by combining dynamic and input matrices, as in equation (20), to obtain a simplified and rapid solution without the integration.

$$\frac{d}{dt}\begin{bmatrix}x(t)\\1\end{bmatrix}=\begin{bmatrix}A_i & B_i\\0 & 0\end{bmatrix}\begin{bmatrix}x(t)\\1\end{bmatrix} \tag{20}$$

or

$$\frac{d}{dt}\hat{x}(t)=\hat{A}_i\hat{x}(t) \tag{21}$$

The solution for the i[th] mode is given by:

$$\hat{x}(t_i)=e^{\hat{A}_i d_i T}\hat{x}(t_{i-1})=\hat{\phi}_i\hat{x}(t_{i-1}) \tag{22}$$

Considering a system with m modes, the state vector for mode m, after the whole period is given by:

$$\hat{x}(t_m)=\hat{\phi}_m\hat{\phi}_{m-1}\dots\hat{\phi}_1\hat{x}(t_0)=\hat{\phi}_{tot}\hat{x}(t_0) \tag{23}$$

where $\hat{x}(t_0)$ is the initial condition and:

$$\hat{\phi}_i=\begin{bmatrix}\phi_i & \Gamma_i\\0 & 1\end{bmatrix}=e^{\hat{A}_i d_i T} \tag{24}$$

The periodic solution can be found assuming that after a complete cycle the state vector is equal to the initial state, as in (25).

$$\begin{gathered}\hat{x}_{per}(t_0+T)=\hat{\phi}_{tot}\hat{x}_{per}(t_0)=\hat{x}_{per}(t_0)\\ \hat{x}_{per}(t_0)=\begin{bmatrix}x_{per}(t_0)\\1\end{bmatrix}\end{gathered} \tag{25}$$

Using (24) to solve (25) gives:

$$x_{per}(t_0)=(I^n-\phi_{tot})^{-1}\Gamma_{tot} \tag{26}$$

where

$$\begin{gathered}\phi_{tot}=\phi_m\phi_{m-1}\dots\phi_1\\ \Gamma_{tot}=(\phi_m\phi_{m-1}\dots\phi_2)\Gamma_1+(\phi_m\phi_{m-1}\dots\phi_3)\Gamma_2\\ +\dots+\phi_m\Gamma_{m-1}+\Gamma_m\end{gathered} \tag{27}$$

Therefore, using equations (17), (22) and (27) the values for all state-variables can be calculated for any t during a cyclic mode.

The average value definition given by (28) can be used to calculate the steady-state values of the state-variables over a cycle.

$$x_{avg}=\frac{1}{T}\int_{t_0}^{t_0+T}x_{per}(t)dt \tag{28}$$

Based on the cyclic description the following system is analysed:

$$\begin{cases}\dot{x}(t)=A_i x(t)+B_i\\ \dot{y}(t)=\dot{x}_{avg}=\dfrac{1}{T}x(t)\end{cases} \tag{29}$$

The augmented vector technique is used again to obtain a simplified solution, as shown in (30).

$$\frac{d}{dt}\begin{bmatrix}x(t)\\1\\x_{avg}(t)\end{bmatrix}=\begin{bmatrix}A_i & B_i & 0\\0 & 0 & 0\\I/T & 0 & 0\end{bmatrix}\begin{bmatrix}x(t)\\1\\x_{avg}(t)\end{bmatrix} \tag{30}$$

Equation (30) can also be represented in a simplified form:

$$\dot{z}(t)=\tilde{A}_i z(t) \tag{31}$$

The averaged state-vector can then be obtained by calculating $z(t_0+T)$ based on the initial state vector $z(t_0)$. Given the initial state vector:

$$z(t_0)=\begin{bmatrix}x_{per}(t_0)\\1\\0\end{bmatrix} \tag{32}$$

The averaged state vector is then calculated:

$$z(t_0+T)=\tilde{\phi}_m\tilde{\phi}_{m-1}\dots\tilde{\phi}_1 z(t_0)=\begin{bmatrix}x_{per}(t_0)\\1\\x_{av}\end{bmatrix} \tag{33}$$

where $\tilde{\phi}_i=e^{\tilde{A}_i d_i T}$.

4.1. Cyclic-averaging analysis for SPS modulation

In this section the cyclic analysis will be shown for forward operation, the same methodology is also applied to the reverse operation.

The state-space description for the forward mode previously obtained from equations (3)-(7) is used as a base for application of the cyclic method. The set of equations can be represented in matrix form as:

$$\frac{d}{dt}\begin{bmatrix}i_{Ls1}\\v_{Cs1}\\i_{Lm}\\v_{Cs2'}\\v_{Cf}\end{bmatrix}=A\begin{bmatrix}i_{Ls1}\\v_{Cs1}\\i_{Lm}\\v_{Cs2'}\\v_{Cf}\end{bmatrix}+B \tag{34}$$

where:

$$\mathrm{A}=\begin{bmatrix}-\dfrac{(r_1+r_2')}{L_{s1}} & -\dfrac{1}{L_{s1}} & \dfrac{r_{C2}'}{L_{s1}} & -\dfrac{1}{L_{s1}} & 0\\ \dfrac{1}{C_{s1}} & 0 & 0 & 0 & 0\\ \dfrac{r_{C2}'}{L_m} & 0 & -\dfrac{(r_{Lm}+r_{C2}')}{L_m} & \dfrac{1}{L_m} & 0\\ \dfrac{1}{C_{s2}'} & 0 & -\dfrac{1}{C_{s2}'} & 0 & 0\\ 0 & 0 & 0 & 0 & -\dfrac{1}{C_f(r_b+r_{Cf})}\end{bmatrix}$$

and

$$B = \begin{bmatrix} \frac{(v_1(t) - nv_2(t))}{L_{s1}} \\ 0 \\ \frac{nv_2(t)}{L_m} \\ 0 \\ \frac{V_{bat} + r_b i_{bridge}}{C_f(r_b + r_{Cf})} \end{bmatrix}$$

The state-variable system depends on the state of voltages $v_1(t)$ and $v_2(t)$. For a converter operating under SPS modulation there are two possible states for each voltage, leading to four operation modes. The periodic behaviour of the bridge voltages v_1 and v_2 for forward operation is shown in Fig. 5, where the four modes can be identified for a cycle. When operating in forward mode the right bridge (v_2) leads and the power flows from the DC bus to the battery.

The beginning of the cycle is considered when the right bridge voltage v_2 becomes positive. The state of the bridges voltages and the output current for the four modes are described in Table 1.

Based on each mode description, the substitution of the values on equation (34) will determine the dynamic matrices A_i and input matrices B_i, where $i = 1, 2, 3, 4$.

In SPS modulation the frequency is fixed and the phase-shift between the output voltage of the two bridges is a known angle between 0 and 90 degrees. Therefore, the duration of each mode is fixed and can be calculated based on the period value and phase-shift angle. The duty cycle for the first mode is then determined as follows:

$$d_1 = \frac{PS}{360} \tag{35}$$

The remaining duty cycles are calculated based on the waveform's symmetry: $d_2 = 0.5 - d_1$, $d_3 = d_1$ and $d_4 = d_2$.

Once the state-space description and mode durations are obtained, the cyclic technique is used to model the converter.

From (26), (32) and (33) the steady-state average values of the state-variables are calculated and, to verify the model over a cycle, the equations (22) and (26) are used for calculation of the values of the state-variables at the beginning of each mode (at times t_0, t_1, t_2 and t_3 in Fig. 5).

4.2. Cyclic-averaging analysis for PPM modulation

For converters operating under PPM modulation the state-variable description from sections 3.1 and 3.2 and matrix representation from equation (34) remain the same. The difference from the previous case is the modes description, now a cycle is divided in eight modes. Considering $\alpha_1 = \alpha_2 = \alpha$, the modes configuration also changes depending on the α range. For this analysis the angle ϕ is considered fixed at ±90° depending on power flow direction.

The operation in forward mode where $90° \leq \alpha \leq 180°$ is presented in Fig. 6. Considering the beginning of a cycle when v_2 becomes positive, the modes description is presented in Table 2.

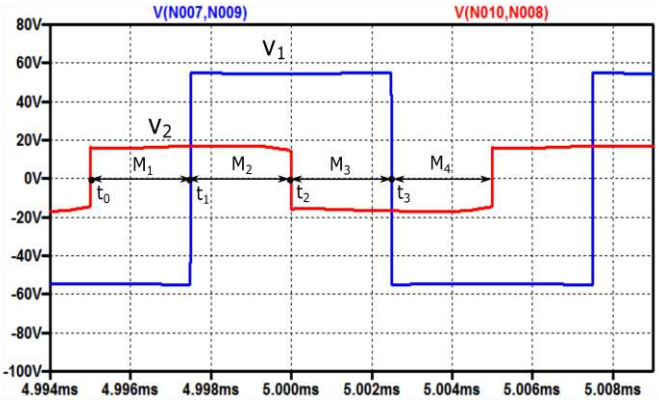

Fig. 5 Typical bridge voltage sequence for SPS operation, forward operation

Table 1 Modes description for SPS modulation case in forward operation

Mode	v_1	v_2	i_{bridge}
M1	$-V_{dc}$	V_{bat}	$n(i_{Ls1} - i_{Lm})$
M2	V_{dc}	V_{bat}	$n(i_{Ls1} - i_{Lm})$
M3	V_{dc}	$-V_{bat}$	$-n(i_{Ls1} - i_{Lm})$
M4	$-V_{dc}$	$-V_{bat}$	$-n(i_{Ls1} - i_{Lm})$

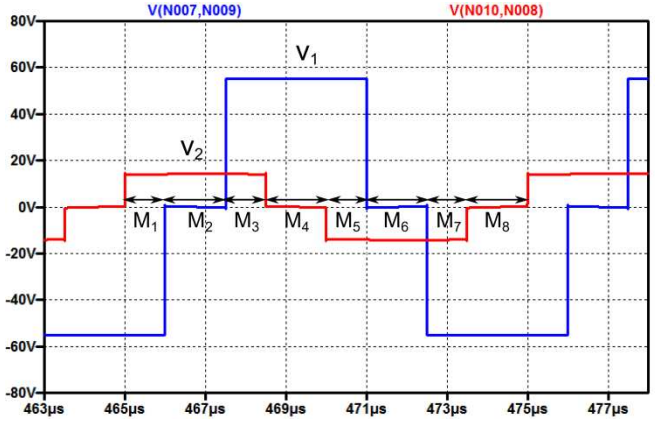

Fig. 6 Typical bridge voltage sequence for PPM operation and $90° \leq \alpha \leq 180°$, forward operation

Table 2 Modes description for PPM modulation when $90° \leq \alpha \leq 180°$, forward operation

Mode	v_1	v_2	i_{bridge}
M1	$-V_{dc}$	V_{bat}	$n(i_{Ls1} - i_{Lm})$
M2	0	V_{bat}	$n(i_{Ls1} - i_{Lm})$
M3	V_{dc}	V_{bat}	$n(i_{Ls1} - i_{Lm})$
M4	V_{dc}	0	0
M5	V_{dc}	$-V_{bat}$	$-n(i_{Ls1} - i_{Lm})$
M6	0	$-V_{bat}$	$-n(i_{Ls1} - i_{Lm})$
M7	$-V_{dc}$	$-V_{bat}$	$-n(i_{Ls1} - i_{Lm})$
M8	$-V_{dc}$	0	0

Since the frequency and phase-shift angles ϕ and α are known, the duties are calculated as follows.

$$d_1 = \frac{-90 + \alpha}{360} = d_3 = d_5 = d_7$$
$$d_2 = \frac{180 - \alpha}{360} = d_4 = d_6 = d_8 \quad (36)$$

Considering now $\alpha \leq 90°$ and forward mode operation, the new configuration of bridge voltages is shown in Fig. 7.

For this case the description of the eight modes is presented in Table 3.

The duties are calculated as in (37).

$$d_1 = \frac{\alpha}{360} = d_3 = d_5 = d_7$$
$$d_2 = \frac{90 - \alpha}{360} = d_4 = d_6 = d_8 \quad (37)$$

When $\alpha = 90°$ the operation is reduced to 4 modes. Both models presented for PPM operation can be used for this case since, according to the duties calculations in equations (36) and (37), the duration of the four modes that are eliminated during 90° operation will be equal to zero.

Similar to the SPS modulation case, the state-variables average values can be calculated using the cyclic modelling equations.

5. Experimental and simulation validation

To verify the models proposed, a converter was designed based on a methodology proposed in [14]. The state-variable and cyclic models described in sections 3 and 4 were simulated in Simulink and MATLAB, with validation of the results being done against a nearly ideal component-based Spice simulation.

After simulation validation, a prototype was built and experimental results are also verified against Spice simulation. The Spice model to experimental validation is modified to include practical values of resistances and inductances.

5.1. Converter design

A 110W, 48-12V, CLLC converter is designed to operate at 100 kHz. The DC voltage conversion ratio is defined in equation (38). The value of DC ratio does not affect significantly the operation of converters under PPM modulation; however, a conversion ratio close to 1 results in considerably higher efficiency and smaller bridge currents for SPS modulated converters, especially for low-power applications [14]. Therefore, the chosen turns ratio n is 4.

$$DC_{ratio} = n\frac{V_{sec}}{V_{pri}} = n\frac{V_{bat}}{V_{dc}} \quad (38)$$

where n is the transformer turns ratio.

The resonant network is tuned to the switching frequency as in (39).

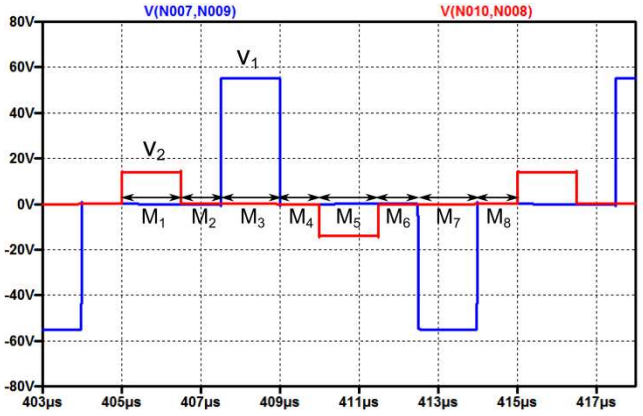

Fig. 7 Typical bridge voltage sequence for PPM operation and $\alpha \leq 90°$, forward operation

Table 3 Modes description for PPM modulation when $\alpha \leq 90°$, forward operation

Mode	v_1	v_2	i_{bridge}
M1	0	V_{bat}	$n(i_{Ls1} - i_{Lm})$
M2	0	0	0
M3	V_{dc}	0	0
M4	0	0	0
M5	0	$-V_{bat}$	$-n(i_{Ls1} - i_{Lm})$
M6	0	0	0
M7	$-V_{dc}$	0	0
M8	0	0	0

$$\omega_r^2 = \frac{1}{(L_{s1} + L_m)C_{s1}} = \frac{n^2}{L_m C_{s2}} = (2\pi f_s)^2 \quad (39)$$

As a result, a base reactance value X_n can be defined:

$$X_n = X_{Cs1} - X_{Ls1} = X_{Lm} = n^2 X_{Cs2} \quad (40)$$

A general output power expression power is obtained based on the modulation angles, as shown in (41), considering the most significant part of the power is transferred at fundamental frequency.

$$P_{out} = \frac{8nV_{dc}V_{bat}}{\pi^2 X_n} sin(\phi)\, sin\left(\frac{\alpha_1}{2}\right) sin\left(\frac{\alpha_2}{2}\right) \quad (41)$$

The modulation angles ϕ, α_1 and α_2 were defined in section 2. For the SPS modulation case the values of α_1 and α_2 are fixed at 180°. The maximum output power can be calculated considering the maximum modulation angles $\phi_{max} = 90°, \alpha_{1,max} = \alpha_{2,max} = 180°$, resulting in:

$$P_{out} = \frac{8nV_{dc}V_{bat}}{\pi^2 X_n} \quad (42)$$

The parameters obtained from this design procedure are listed on Table 4.

5.2. Simulation results and model validation for SPS modulation

Table 4 Parameters values for CLLC converter

Parameter	Value
V_{dc}	48 V
V_{bat}	12 V
C_f, C_i	300 µF
L_{s1}	54.04 µH
C_{s1}	31.24 nF
L_m	27.02 µH
C_{s2}	1.5 µF

The converter was simulated based on the design developed in section 5.1 considering forward and reverse operations. The converter is simulated for phase-shift angles (ϕ) from 10° to 90° in ten degrees steps.

The resistance associated to the filter capacitor is neglected and consequently the output voltage is given by the output filter capacitor voltage, v_{Cf} for forward mode and v_{Ci} for reverse mode. Based on the value obtained for average output voltage and the equivalent circuits, the average output current and power can be calculated from (43) for forward operation and (44) for reverse operation:

$$I_{out} = \frac{v_{Cf,avg} - V_{bat}}{r_b},\ P_{out} = V_{bat} I_{out} + r_b {I_{out}}^2 \quad (43)$$

$$I_{out} = \frac{v_{Ci,avg} - V_{dc}}{r_{dc}},\ P_{out} = V_{dc} I_{out} + r_{dc} {I_{out}}^2 \quad (44)$$

where r_b and r_{dc} are small value resistors in series with the voltage sources.

The average values of output current are measured for both models and compared to results from a LTspice simulation. Results for forward operation are shown in Fig. 8 and reverse operation in Fig. 9.

From figures 8 and 9 it can be noticed that both state-variable and cyclic-averaging models are accurate compared to Spice. For some points the LTspice result is slightly different, mainly due to the difference in precision used for the average voltage calculation in MATLAB/Simulink simulations (4 decimal places) and LTspice simulations (3 decimal places).

To verify the accuracy of the models during a whole cycle, the state-variables values on steady-state were checked at the beginning of each mode, points t_0, t_1, t_2 and t_3 from Fig. 5. In Tables 5 and 6 the results obtained at point t_0 are shown.

The results obtained for the two proposed models are similar to the Spice results. Part of the error is a result of the difficulty to measure the current and voltage values for the LTspice and state-variable models at the exact point in time when each mode starts.

In Table 7 the average execution time for the three models is compared. The results obtained by cyclic-averaging method are directly steady-state while state-variable and Spice models need to be simulated until steady-state is reached, around 7ms. Therefore, for comparison both state-variable and spice models have a simulation time of 8ms with 10ns step size. The execution time when using cyclic-averaging technique is reduced compared to state-variable and Spice models.

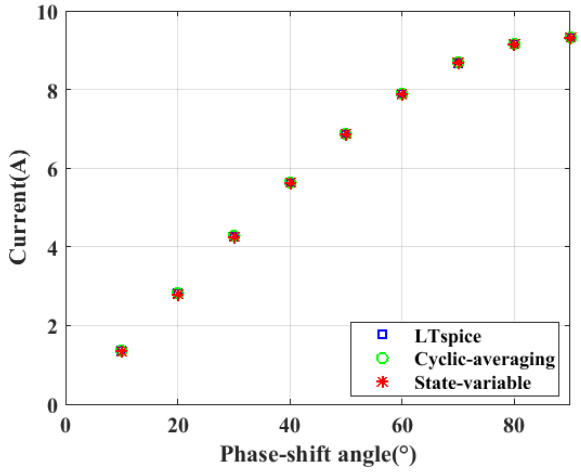

Fig. 8 Simulation results for SPS modulation, forward operation

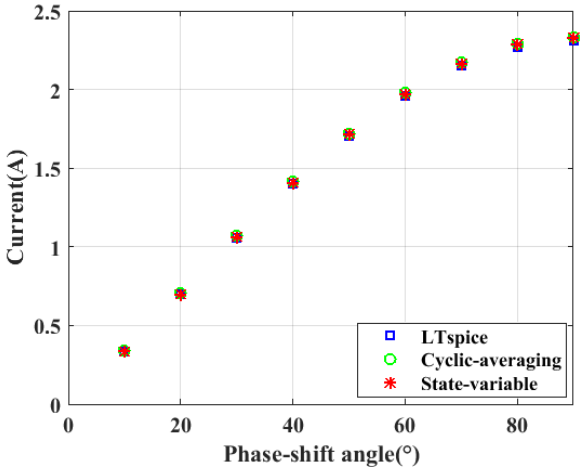

Fig. 9 Simulation results for SPS modulation, reverse operation

Table 5: Variables at t_0 for 90° phase-shift - Forward mode

	Cyclic-averaging	State-variable	LTspice
i_{Ls1}	-3.094 A	-3.097 A	-3.136 A
v_{Cs1}	-3.782 V	-3.967 V	-3.880 V
i_{Lm}	-4.566 A	-4.567 A	-4.597 A
v_{Cs2}	-15.543 V	-15.510 V	-15.536 V

Table 6: Variables at t_0 for 90° phase-shift - Reverse mode

	Cyclic-averaging	State-variable	LTspice
i_{Ls1}	0.490 A	0.506 A	0.490 A
v_{Cs1}	-186.622 V	-186.500 V	-184.696 V
i_{Lm}	-3.582 A	-3.573 A	-3.591 A
v_{Cs2}	-0.935 V	-0.987 V	-0.916 V

Table 7: Comparison of execution time of proposed models for SPS modulation

	Cyclic-averaging	State-variable	LTspice
Execution time (s)	0.005	44.790	25.790

5.3. Simulation results and model validation for PPM modulation

The same simulation analysis made for SPS modulation is repeated for the PPM modulation case. In the PPM case the angle between the bridges is fixed and the output power will be controlled using the phase-shift angle between the bridge legs, α. For this analysis the phase-shift angle α is normalized according to equation (45). Results for forward and reverse operation are presented in Fig. 10 and 11.

$$\alpha_{ratio} = \frac{\alpha}{180°} \tag{45}$$

As for the SPS modulation case, it was observed that both cyclic-averaging and state-variable models are accurate when compared to the Spice model

The values of state-variables are compared between the three models and the results obtained along the cycle are similar, showing the accuracy of the models proposed. In Tables 8 and 9 the variables values at the start of a cycle are presented for the three models. Similarly to the SPS case, there is a small error associated to getting the measurement exactly when each mode starts.

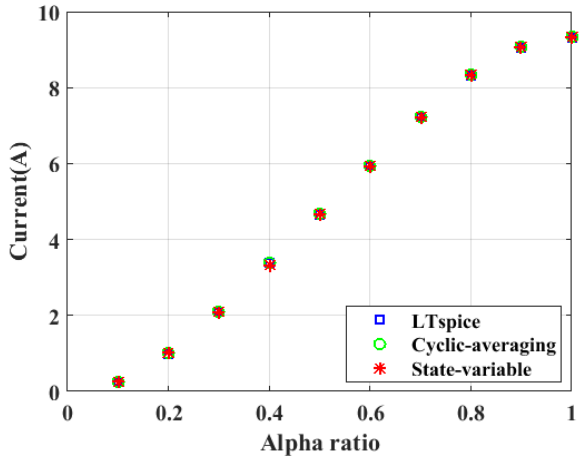

Fig. 10 Simulation results for PPM modulation, forward operation

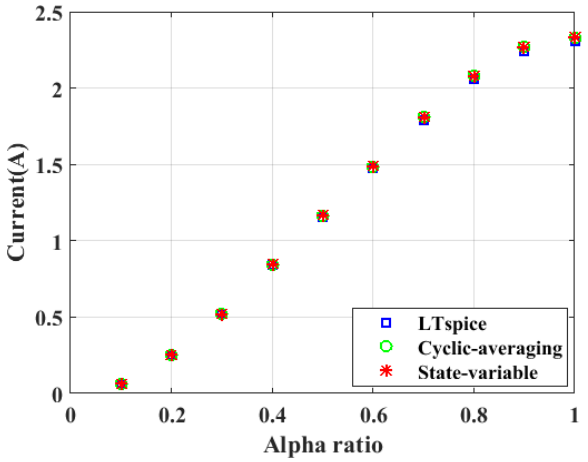

Fig. 11 Simulation results for PPM modulation, reverse operation

The averaged execution times of the models are compared in Table 10. The cyclic-averaging is still the model with the most reduced execution time. Due to the four additional modes on PPM modulation, the simulations of cyclic-averaging and state-variable models are more complex, therefore the execution time is increased compared to the SPS modulation case. The simulation time and step size used for the SPS and PPM case are the same.

For both SPS and PPM modulations cases it was observed that, similar to the output current, the maximum output power is achieved for maximum modulation angles and it decreases with the reduction of the phase-shift angles.

5.4. Prototype results

After the validation by simulation, a prototype was built and simulation and practical results are compared. The difference between designed and practical values is shown in Table 11. The voltage and frequency are still kept at 48-12V and 100 kHz.

For the tests, a 0-60V power supply is used as input. Since the aim of this study is to verify the model of the converter, a resistor, which is simpler to model, is used in the place of the output battery. This way it is not necessary to develop an accurate simulation model for the battery in order to compare simulation and experimental results. The values of resistors are chosen as the equivalent to reproduce a test with an output battery under maximum modulation.

Table 8: Variables at the start of mode 1 for $\alpha_{ratio} = 0.75$ in forward mode

	Cyclic-averaging	State-variable	Ltspice
i_{Ls1}	-1.537 A	-1.529 A	-1.552 A
v_{Cs1}	-156.991 V	-156.900 V	-158.284 V
i_{Lm}	-4.1341 A	-4.128 A	-4.146 A
v_{Cs2}	-5.411 V	-5.392 V	-5.421 V

Table 9: Variables at the start of mode 1 for $\alpha_{ratio} = 0.25$ in forward mode

	Cyclic-averaging	State-variable	Ltspice
i_{Ls1}	0.254 A	0.258 A	0.256 A
v_{Cs1}	-60.695 V	-60.63 V	-60.934 V
i_{Lm}	-0.080 A	-0.071 A	-0.076 A
v_{Cs2}	2.830 V	2.851 V	2.834 V

Table 10: Comparison of execution time of proposed models for PPM modulation

	Cyclic-averaging	State-variable	Ltspice
Execution time (s)	0.008	61.904	23.641

Table 11: Designed and practical values for CLLC prototype

Parameter	Practical values	Theoretical values
L_{s1}	51.844 µH	54.04 µH
C_{s1}	28.408 nF	31.24 nF
L_m	32.089 µH	27.02 µH
C_{s2}	1.355 µF	1.5 µF
n	3.998	4

The cyclic-analysis was modified to consider the load resistors R_{for} and R_{rev} at the output. The output current and power are now calculated using the averaged output filter voltage obtained from the cyclic-averaging method, as in (45) for forward operation and (46) for reverse operation.

$$I_{out} = \frac{v_{Cf,avg}}{R_{for}},\ P_{out} = R_{for}{I_{out}}^2 \tag{45}$$

$$I_{out} = \frac{v_{Ci,avg}}{R_{rev}},\ P_{out} = R_{rev}{I_{out}}^2 \tag{46}$$

where $v_{Cf,avg}$ and $v_{Ci,avg}$ are obtained from the application of (30)-(33) to the cyclic-averaging model.

In SPS modulated converters, the output voltage and current of the converter are controlled by the phase-shift angle between primary and secondary bridges (ϕ), while the power flow direction is controlled by the sign of angle ϕ. When testing a PPM modulated converter, ϕ is kept at $\pm 90°$ and used only to control power flow direction, the output voltage and current is regulated using the phase-shift angles between the legs of each bridge (α). Similar to the simulation analysis, here the prototype was tested in open loop in order to verify a wide range of the phase-shift angles α and ϕ and their influence on the converter's output.

At simulation stage the Spice, cyclic-averaging and state-variable models were simulated in nearly ideal conditions. For comparison with the experimental set-up, the Spice simulation is modified to include the measured values of turns ratio, transformer leakage inductance, resistances of switches, and the non-ideal model of capacitors and inductors including parasitic elements, as shown in Figure 12. The components practical values were measured using the Bode 100 Vector Network Analyser. The cyclic-averaging model is simulated based on the equivalent circuit from Figure 4, therefore only the series resistances, inductances and capacitances are considered. The transformer leakage inductance, parallel resistances and parallel capacitances are neglected at first to avoid modifications in the equation description and increased system complexity.

Since the cyclic-averaging model is derived from state-variable description, both methods have very similar accuracy but the use of cyclic method results in a fast steady-state analysis. Therefore, experimental results are compared to Spice and cyclic-averaging model simulations. The results for forward and reverse operation are shown in Fig. 13 and 14. Both models can successfully predict the behaviour of the converter for variations of phase-shift angle and alpha ratio. However, the cyclic-averaging is not as accurate as the Spice simulation due to the simplifications adopted.

For the implementation of the cyclic-averaging method, the influence of system delays must be considered and incorporated into the duty cycle values calculations, since these delays can cause variations on the phase-shift angles initially implemented. From experimental validation of a converter operating under SPS modulation, it was observed that implementation of small values of phase-shift are subject to reduced precision from the microcontroller and higher influence of delays, contributing to increased errors between simulation and prototype results.

The phase-shift angle ϕ between the primary and secondary bridges is measured for different SPS modulation cases, between 10 and 30 degrees, and an average difference of 3.24° is obtained between the set and measured phase-shift angle. Therefore, the duty cycle equations for the cyclic-averaging method and Spice simulations are modified to take into consideration this angle offset. Explicit modelling of the deadtime was not considered here since this would result in a significantly more complex analysis, with the modification and addition of new operation modes to the cyclic analysis.

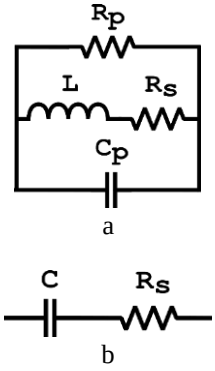

Fig. 12 Non-ideal equivalent circuit
(a) Inductor **(b)** Capacitor

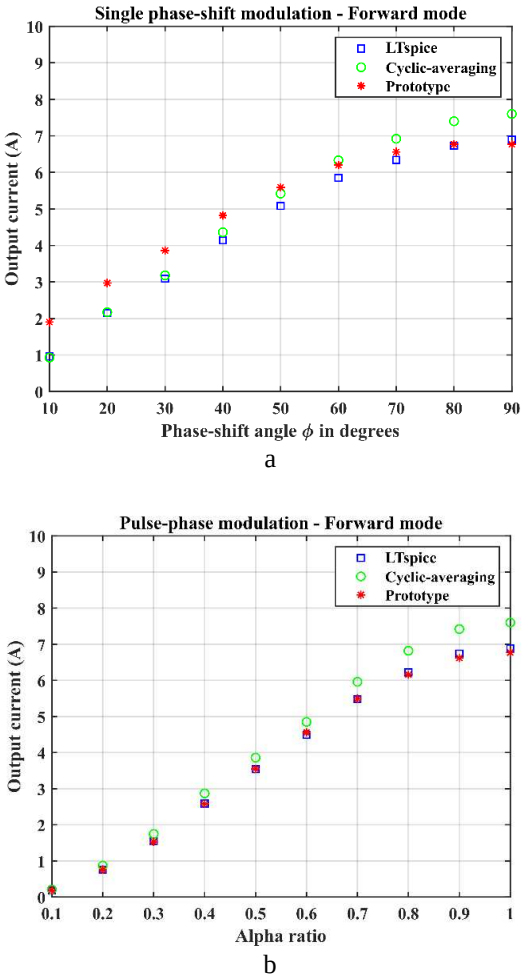

Fig. 13 Comparison between Spice, cyclic-averaging and experimental results in forward mode, $R_{out} = 1.5\Omega$
(a) SPS modulation **(b)** PPM modulation

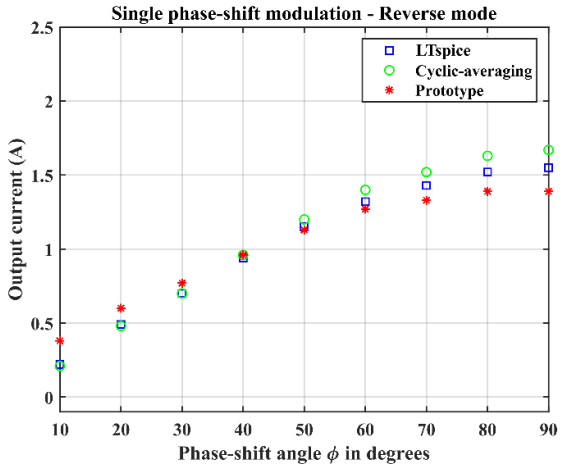

a

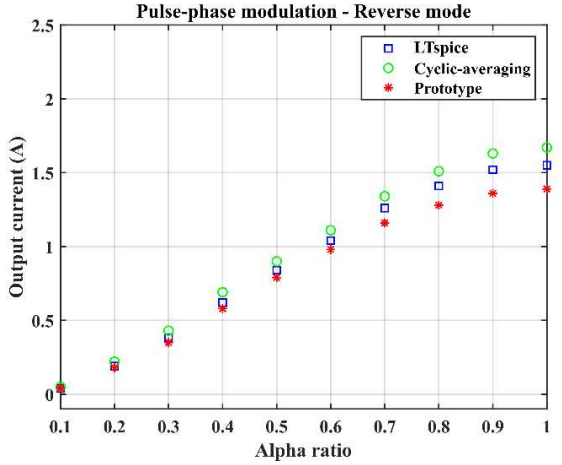

b

Fig. 14 Comparison between Spice, cyclic-averaging and experimental results in reverse mode, $R_{out} = 22\Omega$
(a) SPS modulation **(b)** PPM modulation

According to the soft switching analysis of the phase-shift modulated CLLC converter performed in [17], when using PPM modulation soft switching is only achieved for $\alpha = 180°$. The output current of the secondary bridge is negative when the bridge voltage transitions from negative to positive, resulting in Zero-Voltage Switching (ZVS) operation, while the primary bridge is near Zero-Current Switching (ZCS). As α decreases, ZVS and ZCS no longer occur. For SPS modulated converters, the increase of voltage mismatch between primary and secondary results in high circulation current, hard switching operation and large current spikes, therefore, soft switching is obtained when the ratio between primary and secondary voltages is close to unity. For the investigations performed and all modulation cases analysed, the voltage gain of the resonant tank circuit is closest to unity at maximum modulation and decreases as the phase-shift angles decrease, as shown in Fig. 15 for a PPM modulated converter operating in forward mode.

For a converter operating under PPM modulation, results were not significantly affected by voltage mismatch and delays, even when testing small values of α_{ratio}.

The prototype was not designed and optimized to achieve maximum efficiency, therefore, the circuit's loss elements may significantly influence the results and must be incorporated into the models. To further improve the accuracy of the cyclic method without changing the equation description, the non-ideal inductor circuit from Fig. 12-a can be reduced to an equivalent inductive reactance in series with a resistor and the leakage inductance of the transformer is incorporated to the reactance value of the secondary capacitor. This way, all parasitic elements considered in the Spice simulation are also incorporated to the cyclic method improving the comparison between the models.

The results using the optimized cyclic and Spice models are shown in Fig. 16 and 17. It is observed that the accuracy of the cyclic-averaging model was improved, and results are very close to Spice for both modulation methods.

Considering operation in forward mode at maximum modulation ($\phi = 90°$ and $\alpha_{ratio} = 1$), a difference of 150 mA (2.21%) is measured between Spice and prototype results of output current, while a 200 mA (12.9%) difference is measured for reverse mode.

The simulation results for the SPS modulation test case are now closer to experimental also due to the phase-shift angle compensation implemented. No significant difference is observed for the PPM modulation case.

As previously observed in the simulation analysis, the values of output current, and consequently output power, are maximum for maximum modulation angles and decrease as the phase-shift angles decrease. Therefore, the modulation angles α and ϕ can be used as control variables to regulate the converter.

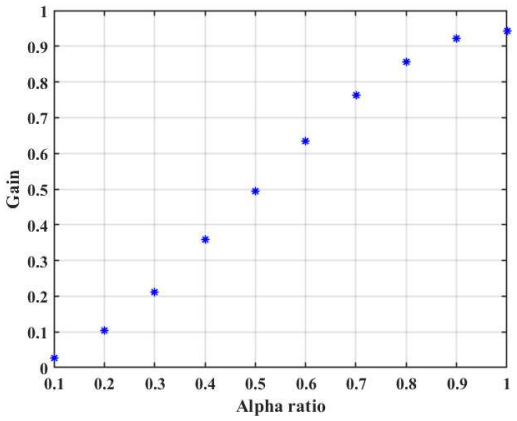

Fig. 15 Voltage gain for PPM modulated converter in forward mode.

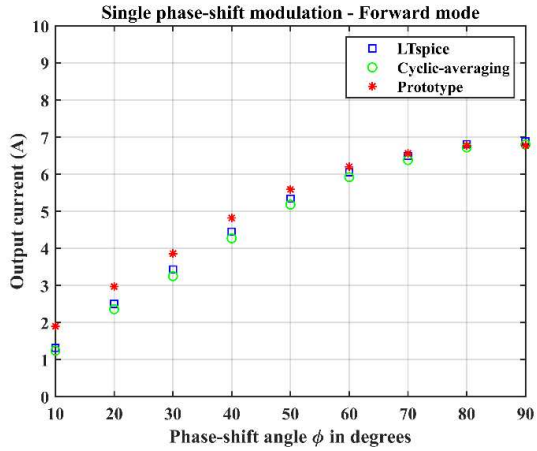

a

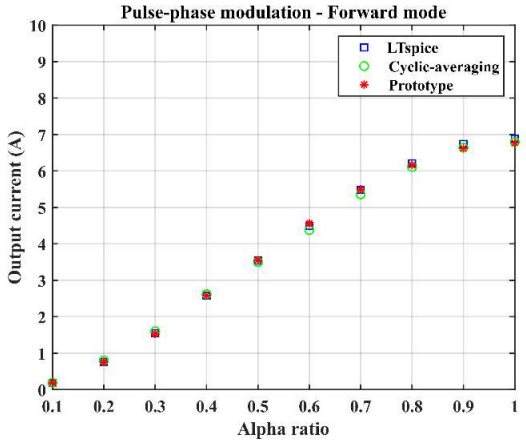

b

Fig. 16 Comparison between Spice, cyclic-averaging and experimental results, optimized models in forward mode, $R_{out} = 1.5\Omega$
(a) SPS modulation **(b)** PPM modulation

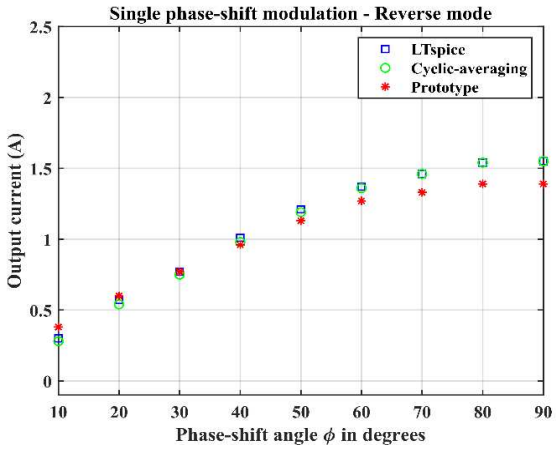

a

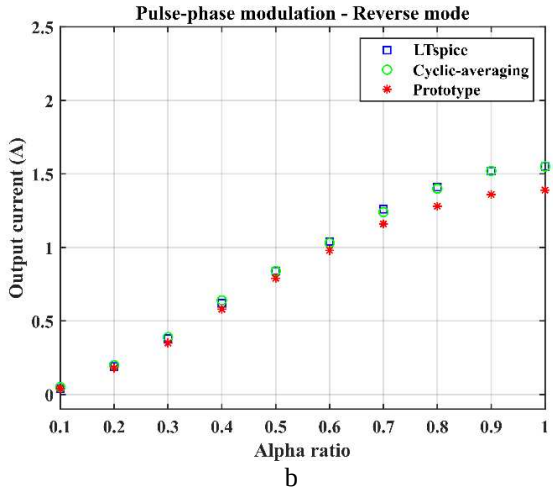

b

Fig. 17 Comparison between Spice, cyclic-averaging and experimental results, optimized models in reverse mode, $R_{out} = 22\Omega$
(a) SPS modulation **(b)** PPM modulation

Even with the delay compensation implemented and addition of parasitic elements to the models, errors between simulation and practical results are lower for the PPM modulation case, due to the increased sensitivity to delays and parasitic elements in the resonant tank when operating under SPS modulation and the difficulty to accurately incorporate the system's delays to the simulation models

Still, it is important to note that other loss elements in the circuit, as wire resistances and inductances, are not included in simulation models, contributing to errors.

To analyse the influence of increased resistances on simulations, considering the maximum modulation case, an addition of 100mΩ on the primary side would result in a decrease of output current of 0.53% (36.1mA) for forward mode and 0.15% (2.3mA) for reverse mode.

Introducing 100mΩ on the secondary, which is the high current side, would result in a change in output current of 0.91% (61.5mA) for forward mode and 5.55% (85.9 mA) for reverse mode. Therefore, reverse mode results, which have low current output, are more significantly affected by additional resistances in the secondary side, also high current side, of the resonant tank.

Overall, the cyclic-averaging method resulted in an accurate analysis, with the advantage of having significantly reduced execution time compared to more traditional methods as Spice and state-variable. Here, the method was applied to evaluate the influence of the phase-shift modulation angles on the converter's behaviour. The cyclic-averaging method can also be used to perform a fast steady-state analysis of the converter during the design and control processes, where the components voltage/current stress and influence of the circuit parameters can be accurately evaluated.

6. Conclusions

In this paper state-variable and cyclic-averaging models were proposed to describe the operation of a bidirectional resonant CLLC converter. The converter is considered operating under two types of phase-shift modulation: single phase-shift and pulse-phase modulation. The models were developed and simulation results were verified against a Spice simulation, showing that both models can be used to accurately predict the behaviour of the CLLC converter under both types of modulation for an ideal design. Furthermore, it was confirmed that the use of cyclic-averaging techniques results in a rapid analysis, with the lowest execution time between the models tested. Experimental results showed reduced error in comparison to both Spice and cyclic-averaging results. Therefore, both models could adequately predict the behaviour of the converter operating under SPS and PPM modulation. It was also observed that converters operating under SPS modulation are more sensitive to delays in the system, and performance deteriorates when testing small phase-shift angles. To reduce errors and improve the system operation, further changes could be done to the system with the addition of iron losses of transformer and wire resistances and inductances to the Spice and cyclic-averaging models, considering a trade-off between accuracy and complexity of the resulting system.

7. Acknowledgements

This work has been supported by CNPq – Brazilian National Council of Scientific Development (Grant: 201065/2015-0).

8. References

[1] Liu, C., Wang, J., Colombage, K., et al.: 'A CLLC Resonant Converter Based Bidirectional EV Charger with Maximum Efficiency Tracking', 8th IET International Conference on Power Electronics, Machines and Drives (PEMD 2016), Glasgow, UK, 2016, pp. 1–6.

[2] Krismer, F., Kolar, J.W.: 'Efficiency-optimized high-current dual active bridge converter for automotive applications', IEEE Transactions on Industrial Electronics, 2012, 59, (7), pp. 2745–2760.

[3] Ferreira, R.J., Miranda, L.M., Araújo, R.E., et al.: 'A new bi-directional charger for vehicle-to-grid integration', 2nd IEEE PES International Conference and Exhibition on Innovative Smart Grid Technologies, Manchester, UK, 2011, pp. 1–5.

[4] Xue, L., Diaz, D., Shen, Z., et al.: 'Dual active bridge based battery charger for plug-in hybrid electric vehicle with charging current containing low frequency ripple', IEEE Transactions on Power Electronics, 2015, 30, (12), pp. 7299–7307.

[5] Oggier, G.G., Garcia, G.O., Oliva, A.R.: 'Modulation strategy to operate the dual active bridge DC-DC converter under soft switching in the whole operating range', IEEE Transactions on Power Electronics, 2011, 26, (4), pp. 1228–1236.

[6] Wang, D., Peng, F., Ye, J., et al.: 'Dead-time effect analysis of a three-phase dual-active bridge DC / DC converter', IET Power Electronics, 2018, 11, (6), pp. 984–994.

[7] Krismer, F., Biela, J., Kolar, J.W.: 'A comparative evaluation of isolated bi-directional DC/DC converters with wide input and output voltage range', Fourtieth IAS Annual Meeting. Conference Record of the 2005 Industry Applications Conference, Kowloon, Hong Kong, 2005, pp. 599–606.

[8] Deng, J., Li, S., Hu, S., et al.: 'Design Methodology of LLC Resonant Converters for Electric Vehicle Battery Chargers', IEEE Transactions on Vehicular Technology, 2014, 63, (4), pp. 1581–1592.

[9] Liu, C., Smieee, J.W., Colombage, K., et al.: 'Current Ripple Reduction in 4kW LLC Resonant Converter Based Battery Charger for Electric Vehicles', 2015 IEEE Energy Conversion Congress and Exposition (ECCE), Montreal, Canada, 2015, pp. 6014–6021.

[10] Foster, M.P., Gould, C.R., Gilbert, A.J., et al.: 'Analysis of CLL voltage-output resonant converters using describing functions', IEEE Transactions on Power Electronics, 2008, 23, (4), pp. 1772–1781.

[11] Gould, C., Bingham, C.M., Stone, D.A., et al.: 'CLL resonant converters with output short-circuit protection', IEE Proceedings-Electric Power Applications, 2005, 152, (5), pp. 1296–1306.

[12] Chen, W., Rong, P., Lu, Z.: 'Snubberless bidirectional DC-DC converter with new CLLC resonant tank featuring minimized switching loss', IEEE Transactions on Industrial Electronics, 2010, 57, (9), pp. 3075–3086.

[13] Malan, W.L., Vilathgamuwa, D.M., Walker, G.R.: 'Modeling and Control of a Resonant Dual Active Bridge with a Tuned CLLC Network', IEEE Transactions on Power Electronics, 2016, 31, (10), pp. 7297–7310.

[14] Twiname, R.P., Thrimawithana, D.J., Madawala, U.K., et al.: 'A Dual-Active Bridge Topology with a Tuned CLC Network', IEEE Transactions on Power Electronics, 2015, 30, (12), pp. 6543–6550.

[15] Zahid, Z.U., Dalala, Z.M., Chen, R., et al.: 'Design of bidirectional DC-DC resonant converter for Vehicle-to-Grid (V2G) applications', IEEE Transactions on Transportation Electrification, 2015, 1, (3), pp. 232–244.

[16] Zou, S., Member, S., Lu, J., et al.: 'Bi-Directional CLLC Converter With Synchronous Rectification for Plug-In Electric Vehicles', IEEE Transactions on Industry Applications, 2017, 54, (2), pp. 1–6.

[17] Malan, W.L., Vilathgamuwa, D.M., Walker, G.R., et al.: 'Novel modulation strategy for a CLC resonant dual active bridge', 9th International Conference on Power Electronics and ECCE Asia (ICPE-ECCE Asia), Seoul, South Korea, 2015, pp. 759–764.

[18] Visser, H.R., van den Bosch, P.P.J.: 'Modelling of periodically switching networks', PESC '91 Record 22nd Annual IEEE Power Electronics Specialists Conference, Cambridge, MA, USA, 1991, pp. 67–73.

[19] Foster, M.P., Sewell, H.I., Bingham, C.M., et al.: 'Cyclic-averaging for high-speed analysis of resonant converters', IEEE Transactions on Power Electronics, 2003, 18, (4), pp. 985–993.

[20] Farias Martins, L., Stone, D.A., Foster, M.P.: 'State-Variable and Cyclic-Averaging Analysis of Bidirectional CLLC Resonant Converters', The Journal of Engineering, 2019, 2019, (17), pp. 4364–4368.

[21] Inoue, S., Akagi, H.: 'A bidirectional DC-DC converter for an energy storage system with galvanic isolation', IEEE Transactions on Power Electronics, 2007, 22, (6), pp. 2299–2306.

[22] Naayagi, R.T., Forsyth, A.J.: 'Bidirectional DC-DC converter for aircraft electric energy storage systems', 5th IET International Conference on Power Electronics, Machines and Drives (PEMD 2010), Brighton, UK, 2010, pp. 1–6.

[23] Kheraluwala, M.H., Gascoigne, R.W., Divan, D.M., et al.: 'Performance characterization of a high-power dual active bridge dc-to-dc converter', IEEE Transactions on Industry Applications, 1992, 28, (6), pp. 1294–1301.

[24] Madawala, U.K., Thrimawithana, D.J.: 'Current sourced bi-directional inductive power transfer system', IET Power Electronics, 2011, 4, (4), pp. 471–480.

[25] Mohamed, A.A.S., Berzoy, A., Nogueira de Almeida, F.G.N., et al.: 'Modeling and Assessment Analysis of Various Compensation Topologies in Bidirectional IWPT System for EV Applications', IEEE Transactions on Industry Applications, 2017, 53, (5), pp. 4973–4984.